ACCSCIENCE PUBLISHING

Materials Science in Additive Manufacturing

ORIGINAL RESEARCH ARTICLE

Laser powder bed fusion of Ni–Fe–Mo permalloy

Nicolas Ayers[1], Nemanja Kljestan[2], Saeyeong Jeon[3], Marko Knezevic[2], Yong Kyu Yoon[3], and Yongho Sohn[1]*

[1]Department of Materials Science and Engineering, University of Central Florida, Orlando, Florida, United States of America

[2]Department of Mechanical Engineering, University of New Hampshire, Durham, New Hampshire, United States of America

[3]Department of Electrical and Computer Engineering, University of Florida, Gainesville, Florida, United States of America

Abstract

Nickel (Ni)–iron (Fe)–molybdenum (Mo) permalloy is a high-permeability soft magnetic alloy widely used for magnetic shielding, yet conventional processing limits geometric complexity. This study evaluates laser powder bed fusion (LPBF) processing of Ni–Fe–Mo permalloy and establishes a process–microstructure–property framework. A systematic parameter study identified an optimal condition of 200 W laser power and 900 mm/s scan speed, producing near-fully dense material (99.65%) with negligible, yet persistent solidification cracking. The as-built microstructure exhibited a pronounced <100> fiber texture and a fine cellular solidification structure with Mo segregation at cell boundaries. Annealing at 1,100 °C reduced microstrain, weakened texture, and partially homogenized segregation through recrystallization. Tensile testing showed that the LPBF-processed material had higher yield strength but lower ductility than wrought permalloy due to residual microcracks. Magnetic measurements confirm soft-ferromagnetic behavior, with annealing reducing coercivity from 83 A/m to 10 A/m while preserving saturation magnetization. These results demonstrate that LPBF-processed Ni–Fe–Mo permalloy is a viable pathway for fabricating complex magnetic shielding components; however, effective crack mitigation and microstructural homogenization would likely require tailored post-LPBF heat treatments and, potentially, targeted alloy composition modifications.

Keywords: Laser powder bed fusion; Additive manufacturing; Soft magnetic material; Permalloy; Microstructure; Mechanical properties

***Corresponding author:**
Yongho Sohn
(Yongho.Sohn@ucf.edu)

Citation: Ayers N, Kljestan N, Jeon S, Knezevic M, Yoon YK, Sohn Y. Laser powder bed fusion of Ni–Fe–Mo permalloy. *Mater Sci Add Manuf*. 2026;5(3):026130021. doi: 10.36922/MSAM026130021

Received: March 26, 2026

Revised: April 18, 2026

Accepted: April 24, 2026

Published online: May 26, 2026

1. Introduction

Nickel (Ni)–iron (Fe)–molybdenum (Mo) permalloy is a soft magnetic alloy that exhibits exceptional sensitivity to weak magnetic fields due to its low coercivity and high magnetic permeability.[1,2] These characteristics enable its widespread use in passive magnetic shielding, transformer cores, and precision electromagnetic components. For transformer cores, permalloy is advantageous because of its low hysteresis losses, while for magnetic shielding, it is valued for its ability to efficiently conduct magnetic flux.[1,3]

Magnetic shielding components play a critical role in mitigating unwanted external magnetic fields in electronic, medical, navigational, and measurement devices, such

as electron microscopes.[4-6] The effectiveness of shielding devices depends not only on the intrinsic, composition-dependent magnetic properties of the shielding alloys—commonly Fe–Ni[7] and Fe–silicon[8]—but also on the geometry and structural design of the shielding component.[9] Conventional manufacturing routes, including cold forming and rolling, impose constraints on achievable geometries, thereby limiting design flexibility and potentially reducing shielding effectiveness.

Laser powder bed fusion (LPBF) has emerged as a prominent additive manufacturing technology for producing structural alloys,[10-12] including aluminum alloys,[13] stainless steels,[14,15] titanium-based,[16] and Ni-based[17] alloys. LPBF offers significant advantages for fabricating complex geometries while maintaining tight dimensional tolerances. Despite the growing adoption of LPBF for high-value metallic systems, the processing of soft magnetic alloys by LPBF remains challenging. These challenges include solidification cracking,[18] crystallographic texture development,[19-21] compositional segregation,[22] and potential degradation of magnetic properties due to rapid solidification.

Recent studies have demonstrated that LPBF-induced microstructures in soft magnetic alloys often differ substantially from those produced through conventional thermomechanical processing, leading to unique combinations of fine cellular substructures, strong crystallographic texture, and elevated residual stresses.[22,23] These features can significantly influence both mechanical integrity and magnetic performance, thereby necessitating careful optimization of processing parameters, post-build heat treatments, and powder chemistry. The addition of 4 to 5 wt. % Mo to an Fe–Ni alloy containing 80 wt.% Ni (hereafter referred to as permalloy) stabilizes the disordered γ-face–centered cubic (FCC) structure and reduces magnetostriction.[3] However, under the steep thermal gradients and rapid solidification inherent to LPBF, Mo exhibits a tendency for microsegregation to interdendritic or cellular boundary regions.[24,25] Local Mo enrichment can introduce compositional fluctuations that increase local magnetocrystalline anisotropy[26] and create elastic strain fields due to solute partitioning. These heterogeneities act as preferential pinning sites for domain wall motion, thereby increasing coercivity and reducing magnetic permeability. In addition, Mo enrichment at cellular boundaries has also been associated with the formation of μ-phase and other topologically close-packed phases in Ni-rich systems, even under highly non-equilibrium solidification conditions.[12] Even at low volume fractions, these phases introduce sharp magnetic and elastic discontinuities that further impede domain wall mobility, serve as crack initiation sites, and degrade the overall performance of permalloy.

Reports on crack formation during LPBF processing of permalloy have not been consistent. Mohamed *et al.*[19] fabricated LPBF permalloy with a maximum relative density of 98.9%. After heat treatment and hot isostatic pressing (HIP), horizontally built tensile specimens exhibited an ultimate tensile strength (UTS) of 364 MPa and an elongation of 5.4%. Traditionally manufactured and annealed permalloy commonly achieves an elongation between 30% and 40%.[27,28] The reason for the low ductility remains unclear; however, the reported fracture surfaces were consistent with brittle intergranular fracture and showed grain separation reminiscent of hot cracking. In a subsequent study, Mohamed *et al.*[23] identified microcracks associated with residual stress accumulation and compositional segregation. These cracks were linked to inferior magnetic performance, particularly increased coercivity, but their effect on tensile behavior was not examined.

In contrast, Li *et al.*[22] reported LPBF fabrication of crack-free permalloy samples with a maximum density of 99.86%. The resulting tensile properties were exceptional, with a UTS and elongation of approximately 725 MPa and 27%, respectively, when tested in the as-built condition with the tensile axis parallel to the build direction. When tested in the direction normal to the build direction, the UTS increased to approximately 750 MPa, and the elongation decreased to 19%. The reduction in elongation was attributed to crystallographic texture, suggesting that specimens loaded in the direction normal to the build direction experienced facilitated Mode I grain boundary separation rather than propagation of fabrication-induced microcracks.

Zou *et al.*[20] identified cracking in LPBF permalloy and distinguished two crack types. Type I cracks propagated predominantly along the build direction and were attributed to thermal stresses generated by cyclic reheating, which promoted intergranular cracking in regions susceptible to segregation of alloying elements and impurities. Type II cracks were randomly oriented with jagged morphologies and exhibited dendritic features on the fracture surface, consistent with solidification cracking. They indicated that both types of cracking were closely related to alloy composition and solidification behavior. Micrographs showed significant solidification cracking in samples printed with moderate to high energy density, corresponding to samples with high relative density and crystallographic texture. Solidification cracking was not apparent in samples with a large fraction of lack-of-fusion flaws, where, coincidentally, columnar grain growth was interrupted by those flaws,

resulting in a reduction of texture. Tensile properties were not investigated in this study. Collectively, these studies suggest that crystallographic texture, solidification cracking, and mechanical performance in LPBF permalloy are strongly coupled; however, a systematic study directly characterizing and linking all of these phenomena has not yet been reported.

In this study, we examined LPBF processing of permalloy with the aim of establishing a detailed process–microstructure–property framework. Building on prior reports of LPBF permalloy processability,[19-23,29] this work systematically examines (i) how scanning parameters and volumetric energy density govern relative density and solidification cracking; (ii) the formation of crystallographic texture and solute segregation under LPBF and the extent to which these features can be modified through post-build annealing; and (iii) the resulting trends in mechanical and magnetic response before and after heat treatment. This study identifies the key constraints and trade-offs associated with LPBF processing of permalloy and provides a foundation for future efforts aimed at crack mitigation, microstructural homogenization, and property optimization.

2. Methods

Gas-atomized permalloy powders were acquired from Aubert and Duval (France). The powder size distribution was determined using an LS 13 320 laser diffraction particle size analyzer (Beckman Coulter, USA). The microstructure of the powders and LPBF samples was examined using a Keyence VHX 7000 optical microscope (Keyence Corp., Japan) and a Zeiss Ultra-55 field emission scanning electron microscope (Carl Zeiss AG, Germany), equipped with an X-ray energy dispersive spectroscopy (XEDS) detector, operating at an accelerating voltage of 20 kV. Microstructures were identified by etching with hydrochloric acid, acetic acid, and nitric acid mixed at a 3:2:1 ratio.

Semi-quantitative analyses from XEDS data were carried out using Noran System 7 Version 3.0 software (Thermo Fisher Scientific Inc., USA) for the quantification of compositions. Phase identification of the powder, wrought, and LPBF samples was carried out using X-ray diffraction (XRD) (PANalytical Empyrean™) with Cu K_α radiation. The XRD patterns were acquired with a step size of 0.03°, a dwell time of 60–90 s, and a 2θ range spanning from 20° to 145°. Diffraction patterns were analyzed using Rietveld refinement implemented in HighScore™ Plus (Version 4.1, Malvern Panalytical, USA) to measure crystallographic texture, peak broadening, and lattice parameters.

Additionally, an SLM 125HL system (Nikon SLM Solutions AG, Germany), equipped with a 400 W, 1,070 nm fiber laser and a beam diameter of approximately 70 μm (IPG Photonics, USA), was used to produce LPBF samples. As presented in Figure 1, cylindrical samples (8 mm in diameter and 10 mm in height) were initially produced by LPBF to evaluate relative density as a function of LPBF parameters. A Ni-based Inconel 718 build plate preheated at 100 °C was used to reduce thermal mismatch. High-purity argon was used as a shielding atmosphere, maintaining an O_2 concentration below 0.1% throughout the build. Laser power (W) and laser scan speed (mm/s) were systematically and independently varied as listed in Table 1. A hatch spacing of 0.12 mm, a layer thickness of 0.03 mm, a stripe scanning strategy with a stripe width of 10 mm, a stripe overlap of 0.08 mm, and a 67° rotation between layers were held constant for this study. Contouring, up-skin, and down-skin parameters were not employed. Each cylindrical sample was sectioned parallel and perpendicular to the build direction, as schematically illustrated in Figure 1, and metallographically prepared for microstructural analysis by optical and electron microscopy.

Figure 1. Schematic illustration and a representative photograph of the printed cylinder, indicating the sectioning directions used for microstructure analysis

Table 1. Laser powder bed fusion parameters used for density optimization and the relative density of each sample

Laser power	Laser scan speed (mm/s)	Energy density (J/mm³)	Relative density (%)
125 W	200	173.6	91.45 ± 3.15
	400	86.8	99.21 ± 0.35
	600	57.9	98.06 ± 2.78
	700	49.6	98.04 ± 0.42
	800	43.4	94.90 ± 1.99
	900	38.6	96.14 ± 1.48
	1,000	34.7	91.33 ± 2.45
200 W[a]	200	277.8	90.67 ± 2.80
	400	138.9	95.86 ± 2.18
	600	92.6	99.59 ± 0.14
	700	79.4	99.68 ± 0.05
	800	69.4	99.69 ± 0.10
	900[a]	61.7[a]	99.65 ± 0.10[a]
	1,000	55.6	99.36 ± 0.35
	1,200	46.3	97.51 ± 0.61
	1,400	39.7	95.60 ± 1.26
	1,600	34.7	91.97 ± 1.6
	1,800	30.9	88.90 ± 2.06
	2,000	27.8	84.81 ± 1.83
	2,200	25.3	84.11 ± 1.41
300 W	200	416.7	89.51 ± 4.44
	400	208.3	96.93 ± 0.63
	600	138.9	99.28 ± 0.39
	700	119.0	99.22 ± 0.24
	800	104.2	99.66 ± 0.08
	900	92.6	99.68 ± 0.18
	1,000	83.3	99.60 ± 0.17
	1,200	69.4	99.15 ± 0.24
	1,400	59.5	98.55 ± 0.34
	1,600	52.1	96.54 ± 1.44
	1,800	46.3	93.79 ± 1.95
	2,000	41.7	93.21 ± 1.61
	2,200	37.9	92.89 ± 1.03
350 W	400	243.1	94.32 ± 2.13
	600	162.0	99.31 ± 0.12
	700	138.9	99.22 ± 0.38
	800	121.5	99.23 ± 0.36
	900	108.0	98.83 ± 0.31
	1,000	97.2	99.79 ± 0.15
	1,200	81.0	99.23 ± 0.28
	1,400	69.4	99.17 ± 0.25
	1,600	60.8	98.72 ± 0.51
	1,800	54.0	97.14 ± 0.32
	2,000	48.6	97.61 ± 0.50
	2,200	44.2	95.22 ± 0.50

Notes: Slice thickness, hatch spacing, and scan rotation were held constant at 0.03 mm, 0.12 mm, and 67°, respectively. [a]The experimentally identified optimal parameter.

Optical micrographs acquired at 100× magnification were analyzed using ImageJ software (Version 1.53t, National Institutes of Health, USA). Flaw density was quantified at five locations on the cross-sectional plane normal to the build direction: top-left, top-right, center, bottom-left, and bottom-right. Flaw density was defined as the area fraction of dark-contrast features. Crack density was determined from the same micrographs using the "skeletonize" tool; after contrast thresholding, images of two-dimensional defect cross-sections were iteratively eroded into one-dimensional lines using this tool. The total line length was then summed and divided by the image area to calculate crack density in units of μm^{-1}.

To better understand the phase constituents and microstructural development of LPBF permalloy, a wrought alloy (purchased from EFINEA Metals [USA] under the trade name "Alloy 79," conforming to ASTM A753 Alloy Type 4 standards) with the same composition was examined. In addition, annealing of LPBF permalloy

was performed by encapsulating samples in a quartz tube that was evacuated to 10^{-6} Torr and subsequently backfilled with ultra-high-purity argon before sealing. The sealed tubes were placed in a tube furnace and heated to 1,100 °C, held for 2 h, then cooled to 600 °C at 100 °C/h, followed by cooling to 350 °C at 200 °C/h, and finally air-cooled to room temperature.

For mechanical testing, six tensile bars conforming to ASTM E8/E8M were fabricated using the density-optimized laser parameter identified in this study. All tensile bars were manufactured in a horizontal build direction, as shown in Figure 2. Samples were removed from the build plate by removing the sacrificial support structures, and the gauge sections were polished to 1,200 grit using silicon carbide grinding papers to ensure a consistent surface finish. Room-temperature uniaxial tensile tests were conducted quasi-statically using an MTS Landmark 370 testing system (MTS Systems Corporation, USA) equipped with a 250 kN load cell. A static axial clip-on extensometer was affixed to the gauge section, and tests were performed at a nominal strain rate of 10^{-3}/s. Three as-built and three heat-treated samples were tested in tension. Fracture surfaces were subsequently examined using field emission scanning electron microscopy to identify crack initiation sites and assess the relationship between heat treatment and mechanical failure modes.

Magnetic measurements were performed with a MicroSense® EV9 vibrating sample magnetometer (VSM; MicroSense, USA) with a maximum applied field of approximately 200 kA/m. All measurements were

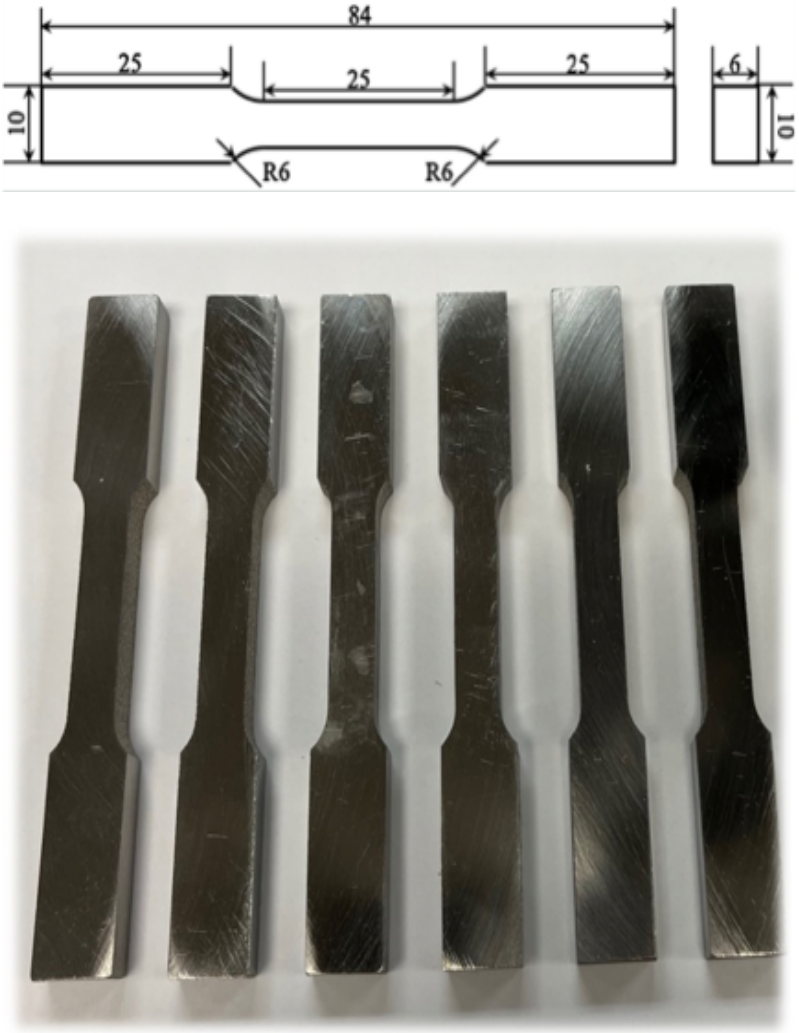

Figure 2. Schematic illustration (dimensions in mm) and a representative photograph of the tensile test specimens fabricated by laser powder bed fusion

conducted at room temperature (24 °C). Cylindrical as-built and heat-treated samples were sectioned into thin discs (5 mm in diameter and 0.3–0.6 mm in thickness). Permalloy's high permeability makes it sensitive to demagnetizing fields dependent on sample geometry. To compensate for this phenomenon, a demagnetization factor was calculated and applied[30,31] to determine the magnetic properties of samples.

3. Results

3.1. Laser powder bed fusion

Figure 3 presents the typical characteristics of the permalloy powders. Particles were generally spherical with few satellites and no visible oxidation, as shown in Figure 3A. The powders exhibited an equiaxed grain structure with occasional gas-trap pores (Figure 3B) and a bimodal size distribution (D10 = 24.55 µm, D25 = 29.57 µm, D50 = 38.36 µm, D75 = 50.54 µm, D90 = 60.48 µm) (Figure 3C). The composition of the as-received powders, measured by XEDS, was 79.87 ± 0.49 wt.%, 15.62 ± 0.22 wt.%, and 4.50 ± 0.29 wt.% for Ni, Fe, and Mo, respectively. Flow testing with a Hall flow measurement yielded good flowability, with a flow time of approximately 5 s per 50 g.

Optical micrographs from the XZ cross-sections of samples produced for LPBF optimization are presented in Figures 4 and 5. Similar to other metallic alloys produced by LPBF, excessive energy density yielded keyhole porosity and solidification cracking (Figure 5A), whereas insufficient energy density produced lack-of-fusion defects (Figure 5B). Appropriate and intermediate energy density produced near-fully-dense permalloy; however, a small amount of hairline cracking was observed (Figure 5C).

Relative density as a function of LPBF parameters measured via quantitative image analysis is presented in Table 1 and Figure 6A. Using a laser power of 200 W with a wide range of scan speeds yielded a near-full-density alloy. Notably, solidification cracking was still observed, although rarely, even when processed at a laser power of 200 W. Figure 6B presents crack density measured via quantitative image analysis. A laser power of 200 W and a scan speed of 900 mm/s were identified as the optimal LPBF parameter set, based on high relative density and low crack density, and were used for the fabrication of mechanical and magnetic test samples.

3.2. Phase constituents and microstructure

X-ray diffraction was carried out for the powder, wrought, as-built, and annealed permalloy samples, as shown in Figure 7. All samples exhibited an FCC solid–solution XRD pattern with no other phases detected. The powder exhibited the highest intensity at the (111) peak. The wrought–annealed alloy displayed similar relative peak intensities to the powder, indicating a randomly oriented grain structure. In contrast, the as-printed specimen exhibited a markedly higher (200) intensity relative to (111), consistent with preferential solidification growth along the <100> direction in FCC Ni-based alloys during solidification.

Following annealing, the (111) peak became the most intense, although the intensity ratio (i.e., I_{111}/I_{200}) remained lower, around 1.75, than that of the powder (~3), indicating that some recrystallization and twinning had occurred during annealing. The lattice parameter, determined by Nelson–Riley analysis, was 3.555 Å for the as-printed sample and 3.554 Å for the annealed sample. The full width at half maximum, obtained from the high-angle (331) reflection for the as-printed and annealed samples, was measured at 0.494° and 0.251°, respectively.

Figure 8 presents micrographs of as-built and annealed permalloy. In the as-printed condition, a cellular sub-grain microstructure was observed with intercellular segregation of Mo and Fe, as shown in Figure 8A. Melt pool boundaries were visible in a stacked semicircular pattern characteristic of LPBF. However, unlike typical LPBF microstructures, large columnar grains extended across multiple melt pools along the build direction, as shown in Figure 8B. Persistent solidification cracks were observed along the grain boundaries parallel to the build-direction (i.e., Z-direction). Figure 8C shows that, after annealing heat treatment, the cellular segregation was dissolved, and recrystallization twins appeared. Discontinuous strings of selective etch pits were observed in the annealed sample, as shown in Figure 8C, outlining features resembling the original impurity- or solute-enriched cellular and grain boundaries.

3.3. Mechanical and magnetic properties

Figure 9 shows the engineering stress–strain curves of LPBF permalloy in the as-printed and annealed conditions. The as-printed samples exhibited a yield strength (YS) of 471 ± 1 MPa and a UTS of 552 ± 7 MPa. Annealed samples showed a reduced YS of 232 ± 2 MPa and a UTS of 433 ± 9 MPa. The reduction in strength after annealing was attributed to dislocation annihilation and dissolution of the fine cellular solidification microstructure. However, the expected increase in ductility typically associated with stress-relief annealing was not observed. Both as-printed and annealed samples exhibited elongations of approximately 10%, which were limited by residual hot cracking introduced during LPBF. Comparatively, traditionally processed and annealed permalloy has a typical YS of 220 MPa, UTS of 580 MPa, and elongation of 40%.[28]

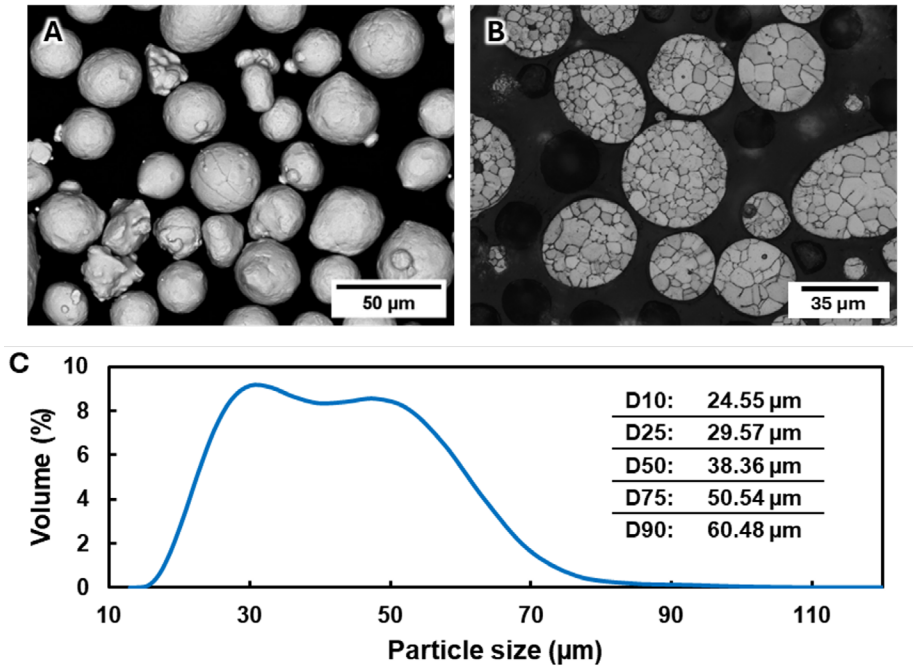

Figure 3. Characterization of permalloy powder feedstock. (A) Secondary electron micrograph of powder morphology (scale bar = 50 µm, magnification = 500×), (B) optical micrograph of the etched powder cross-section morphology (scale bar = 50 µm, magnification = 1,500×), and (C) particle size distribution.

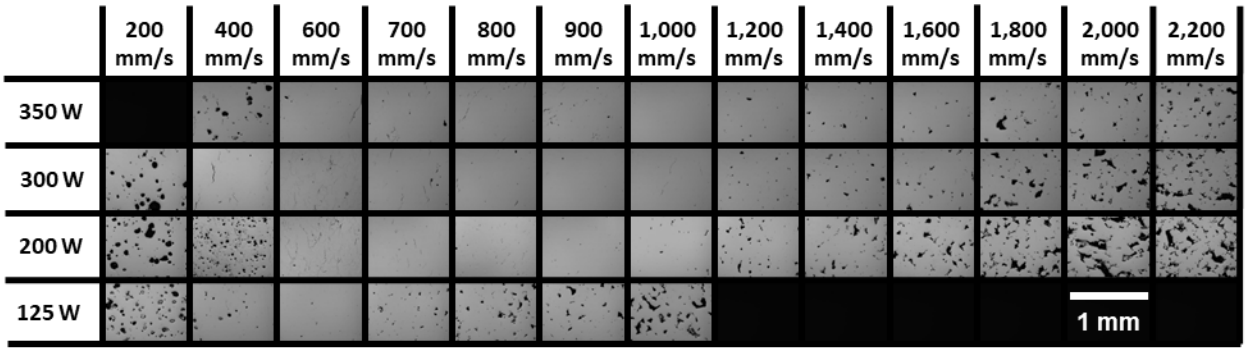

Figure 4. Representative optical micrographs of samples produced using each laser power–scan speed combination during the initial laser powder bed fusion density optimization

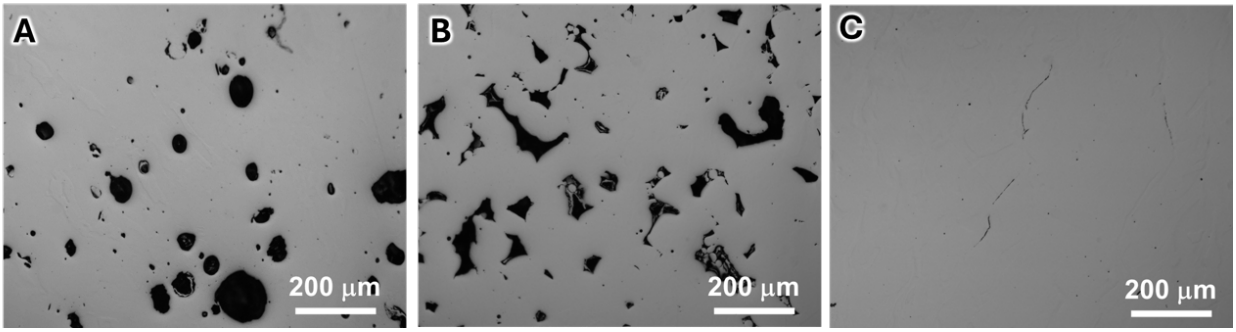

Figure 5. Typical microstructural features in laser powder bed fusion permalloy: (A) keyhole pores, (B) lack-of-fusion flaws, and (C) solidification cracks (scale bar = 200 µm, magnification = 100×).

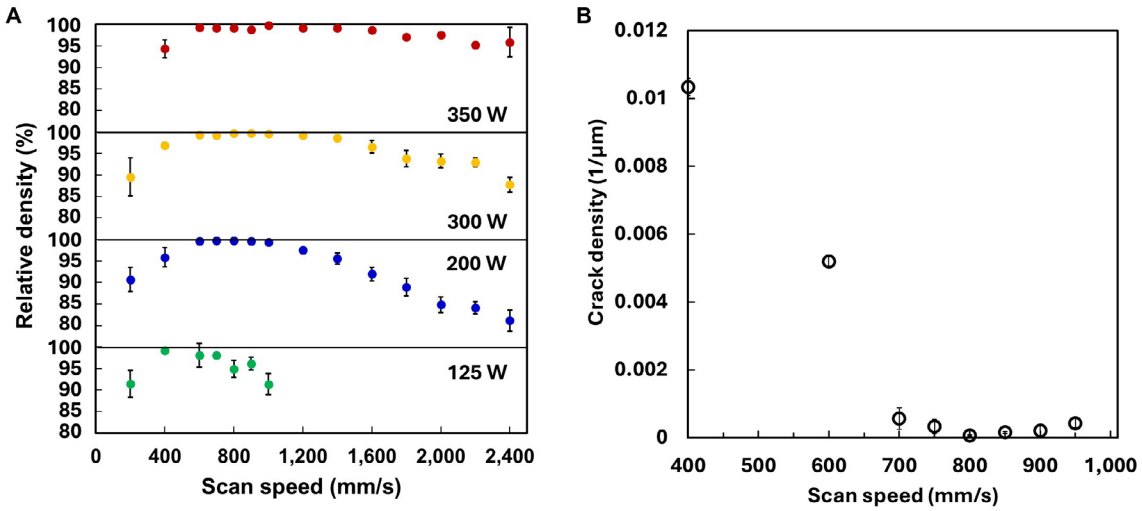

Figure 6. Influence of laser parameters on flaw formation. (A) Relative density measurements from the initial parameter optimization, and (B) crack density for the 200 W series of samples.

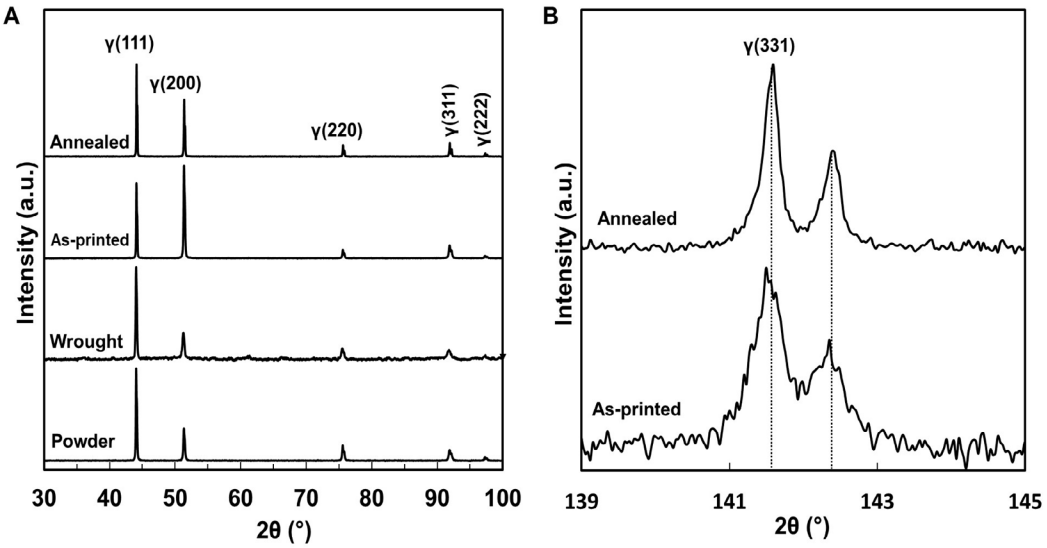

Figure 7. X-ray diffraction patterns for permalloy in the powder, wrought, as-printed, and annealed conditions for (A) 2θ range of 30–100°. (B) High-angle (331) diffraction peak showing no peak shift and reduced peak broadening after annealing.

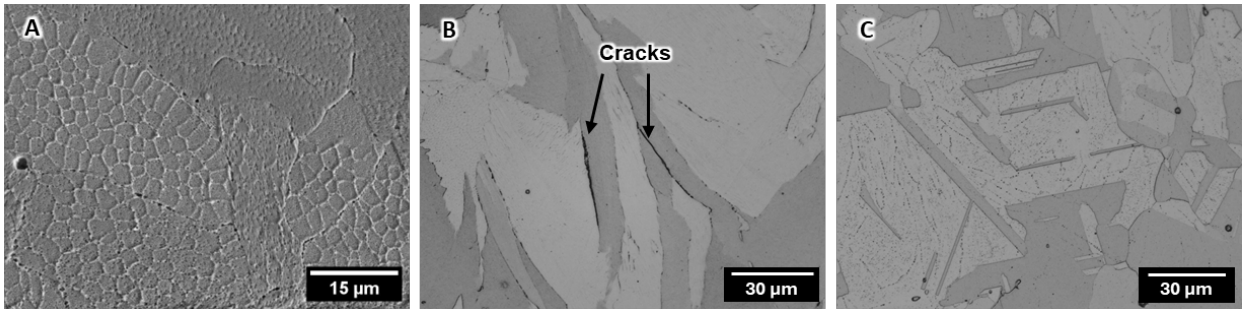

Figure 8. Microstructure of permalloy. (A) Backscattered image of as-printed permalloy highlighting the cellular solidification morphology (scale bar = 15 μm; magnification = 2,000 ×). Optical micrographs of (B) as-printed (scale bar = 30 μm; magnification = 2,000 ×) and (C) annealed permalloy (scale bar = 30 μm; magnification = 1,500 ×).

The fracture surface characteristics, as shown in Figure 10, substantiate the findings from the mechanical properties. In the as-printed condition, the fracture surface consisted of dimples and fan-like cleavage planes, indicating a mixed-mode fracture (Figure 10A and 10B). In addition, Figure 10A shows defects from the printing process that are visible on the fracture surfaces. They were spherical pores corresponding to keyhole or gas-trap pores seen in the cross-section, which were persistently observed in small amounts even in samples produced using optimal LPBF parameters. Because of their orientation relative to the tensile axis, hot cracks would exhibit an opening K_I mode fracture, allowing a view of one side of the internal crack on the fracture surface shown in Figure 10C. The hot crack that propagated in tension displayed a cellular solidification surface morphology. Similar results have been reported from the fracture surface analysis of LPBF Haynes 230 alloy.[32]

For the annealed samples, the tensile fracture surface exhibited a brittle, intergranular fracture morphology, as shown in Figure 10D. Particles rich in Fe and Mo were frequently observed on the annealed sample fracture surface (Figure 10D). XEDS from these particles showed an enrichment of Mo measured at 31.71 ± 0.6 wt. %, compared to the bulk Mo concentration of 4.79 ± 0.47 wt. %. Exact concentrations of these particles could not be determined due to their relatively small size compared to the X-ray interaction volume.

The magnetic behavior of wrought and LPBF Ni–Fe–Mo permalloy samples was characterized by VSM, as shown in Figure 11. The wrought permalloy exhibited a saturation magnetization of 531 kA/m and a coercivity of 105 A/m. The as-printed LPBF permalloy showed a saturation magnetization of 475 kA/m and a coercivity of 83 A/m. After annealing, the LPBF material retained a similar saturation magnetization (473 kA/m) and exhibited a remarkably reduced coercivity of 10 A/m.

4. Discussion

Laser powder bed fusion optimization of permalloy exhibited typical process–defect relationships regarding keyhole porosity, lack-of-fusion defects, and solidification cracking. At low scan speeds combined with high laser power, transition to keyhole-mode melting generated deep vapor depressions and associated pore chains, consistent with observations in Ni-based alloys processed under excessive energy input.[17,33,34] In addition to keyhole porosity, these high energy densities also increased susceptibility to solidification cracking, attributable to steep thermal gradients and solute-enriched interdendritic liquid films,[32] which persist for longer periods due to excessive heating.

Two types of cracking are commonly observed during LPBF: solid-state (cold) cracking and solidification (hot) cracking.[35] Solid-state cracking arises from the fracture of brittle phases that are unable to accommodate the thermomechanical stresses that develop during processing. Solid-state cracking presents a significant challenge to the LPBF fabrication of tool steels,[36] where a high volume fraction of carbides promotes brittleness, and in refractory alloys,[37] which exhibit elevated ductile-to-brittle transition temperatures. Permalloy, however, is not susceptible to solid-state cracking given its single-phase FCC microstructure and inherent ductility; instead, the interdendritic and cellular features observed on the fracture surfaces in this work indicate the presence of solidification cracking, even under optimized processing parameters.

Solidification cracking arises when the strain generated by solidification shrinkage and subsequent thermal contraction cannot be accommodated plastically by the partially solidified alloy system.[32,38-40] As the solid fraction approaches unity, the solid phase undergoes thermal contraction while the remaining thin liquid films along grain boundaries provide insufficient cohesion, promoting intergranular separation. At this stage, both the liquid volume and available time are inadequate for grain coalescence or liquid backfilling. This mechanism is commonly associated with columnar grain structures formed during LPBF,[18,41] and was similarly observed in the present work.

A simple but commonly used metric for assessing solidification cracking susceptibility, proposed by Kou,[40] expressed as $|dT/d(f_S^{1/2})|$ near $(f_S)^{1/2} = 1$, predicts increasing cracking tendency with larger values. Hyer *et al.*[42] demonstrated that solidification cracking in aluminum–Si alloys, as a function of Si concentration, correlates well with this index. Applying a similar approach using Scheil solidification curves simulated in Thermo-Calc, as shown in Figure 12, the cracking susceptibility index for permalloy was estimated to be approximately 1,403 °C. This value is substantially lower than those reported for several Ni- and Fe-based alloys that are routinely fabricated, crack-free, by LPBF (IN625: 4,344 °C; IN718: 4,975 °C; 316L: 4,523 °C; 17-4PH: 3,061 °C). The presence of microcracking in LPBF-processed permalloy, despite its comparatively low predicted susceptibility, indicates that this criterion alone is insufficient. This discrepancy likely reflects process- and alloy-specific effects not captured by the metric, including grain nucleation versus growth, strain accumulation under extreme thermal gradients, melt-pool geometry effects, and limited solidification-stage strengthening mechanisms available to accommodate thermal strain.

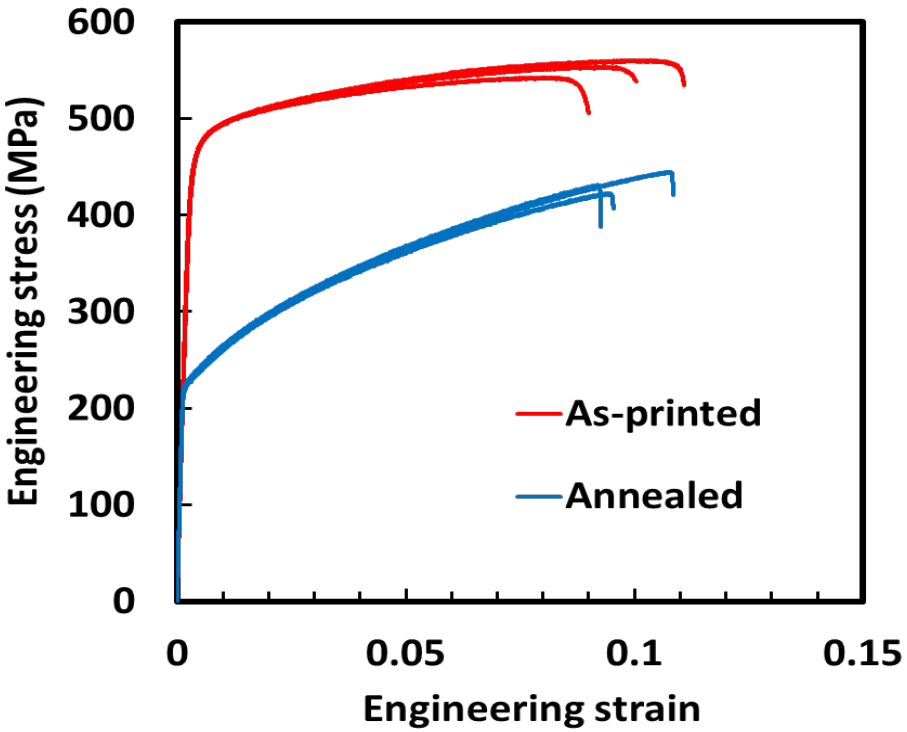

Figure 9. Engineering stress–strain curves of as-printed and annealed permalloy produced using optimal laser powder bed fusion parameters

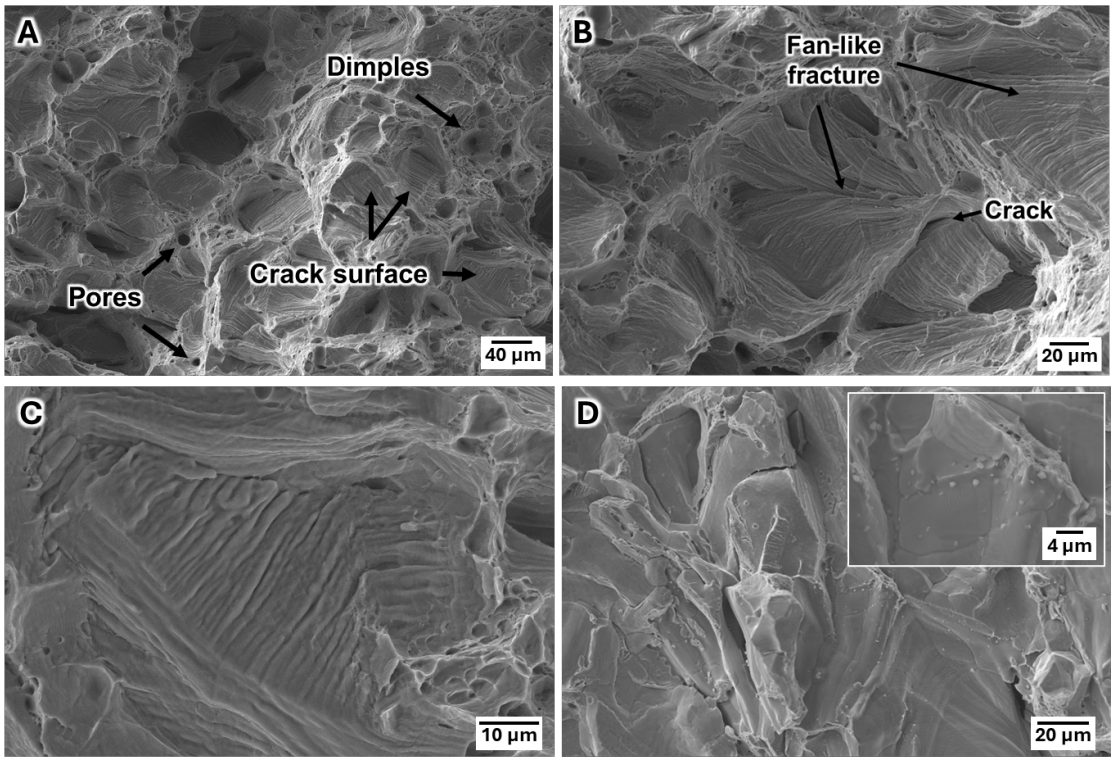

Figure 10. Fracture surfaces of the (A–C) as-printed (A. scale bar = 40 µm, magnification = 200 ×; B. scale bar = 20 µm, magnification = 400 ×; C. scale bar = 10 µm, magnification = 1,250 ×) and (D) annealed permalloy tensile specimens (scale bar = 20 µm, magnification = 500 ×). The inset image shows iron- and molybdenum-rich particles decorating the fracture surface of the annealed permalloy (scale bar = 4 µm, magnification = 3,000 ×).

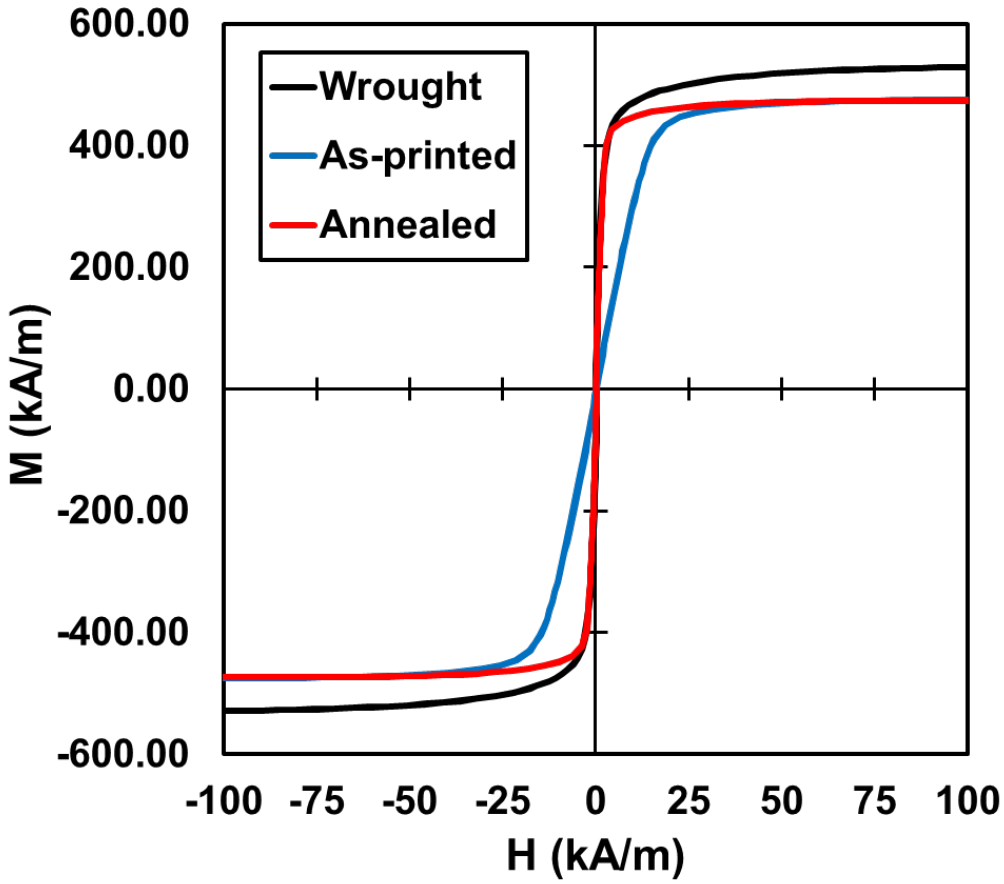

Figure 11. Magnetization–field (M–H) hysteresis loops of wrought, as-printed, and annealed samples measured using a vibrating sample magnetometer

Increasing scan speed generally lowers the effective energy input, thereby suppressing keyhole-mode melting and reducing thermal gradients. Consistent with this behavior, higher scan speeds led to a reduction in both pore formation and crack density (Figure 4). However, at excessively high scan speeds (>1,400 mm/s), insufficient energy delivery resulted in incomplete melting of the powder feedstock and the emergence of lack-of-fusion defects. These findings indicate that defect formation in LPBF-processed permalloy is governed by the coupled effects of rapid solidification, solute segregation, grain growth, and thermal-gradient–driven stress accumulation. An optimal processing window, centered at approximately 200 W laser power and 900 mm/s scan speed, provided the most favorable balance among these competing defect mechanisms, producing dense microstructures (>99.6%) with minimal cracking.

The as-built microstructure was characterized by a fine cellular solidification network with Mo enrichment at cell boundaries and a pronounced <100> fiber texture, reflected by strong (200) diffraction intensity. These features are consistent with rapid solidification phenomena and steep thermal gradients that promote columnar grain growth along the build direction, a morphology frequently observed in LPBF alloys exhibiting hot-cracking susceptibility.[18] The preferential segregation of Mo to cellular boundaries is expected to facilitate the formation of solute-rich interdendritic liquid films, which are widely implicated in solidification cracking behavior.

Annealing at 1,100 °C produced significant modification of the LPBF microstructure, including dissolution of the cellular segregation network and attenuation of the as-built <100> preferred orientation through recrystallization and annealing twinning. The concurrent narrowing of diffraction peaks following annealing is consistent with reduced microstrain and a lower dislocation density. However, the heat treatment employed in this study (i.e., based on conventional permalloy processing conditions) failed to completely remove the residual compositional heterogeneities and to introduce twin boundaries that may act as obstacles to domain wall motion.[43] Thus, a modified heat treatment tailored for LPBF alloys is warranted,

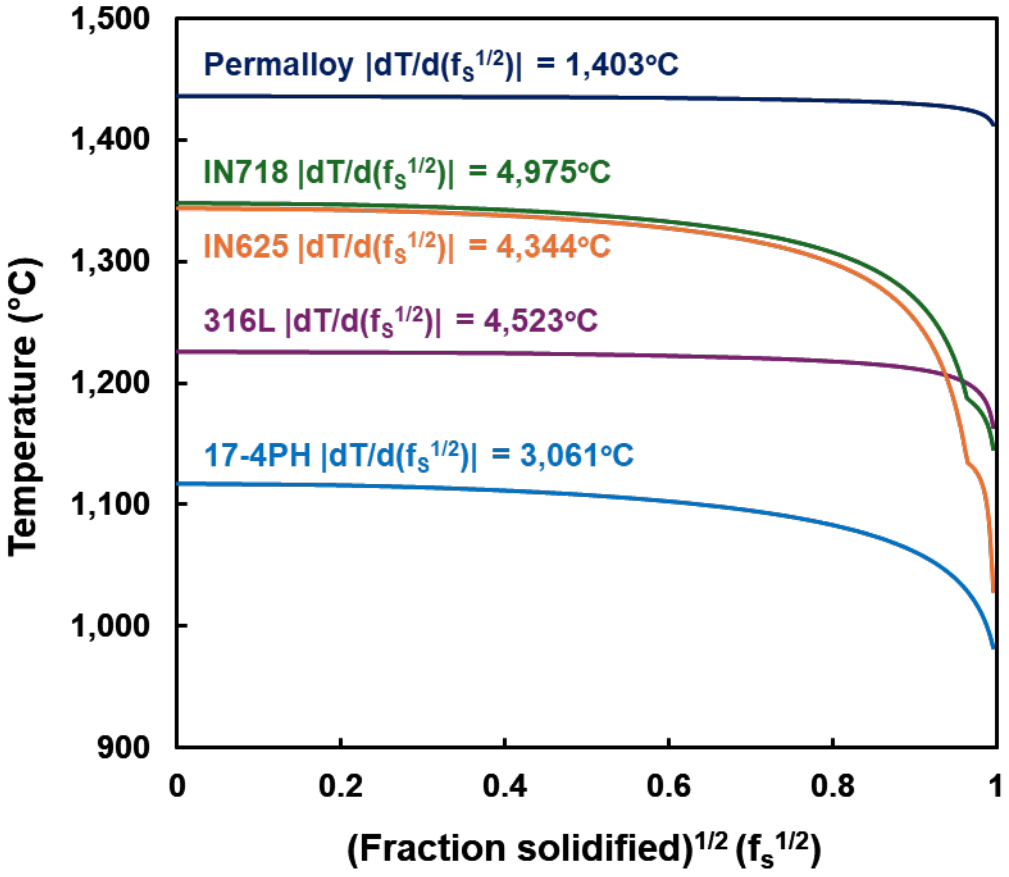

Figure 12. Temperature versus fraction solidified ($f_S^{1/2}$) solidification curves comparing permalloy with selected nickel- and iron-based alloys commonly fabricated by laser powder bed fusion (IN718, IN625, 316L, and 17-4PH). The maximum slope, $|dT/d(f_S^{1/2})|$, was used as the cracking susceptibility index. The curves were simulated using Thermo-Calc 2024b with the TCNI12 and TCFE13 databases.

since the commercially specified annealing treatment was effective in mitigating residual stress and weakening texture, but insufficient for fully optimizing the soft-magnetic performance of LPBF permalloy.

Further improvements in both mechanical and magnetic properties may be achieved through HIP, which would eliminate internal defects, including cracks, enhance diffusion-driven homogenization of cellular segregation, and reduce dislocation density,[23] thereby decreasing the density of domain-wall pinning sites. In addition, annealing in a hydrogen atmosphere can remove oxygen and other interstitial impurities; an approach that is expected to reduce coercivity.[44]

Mechanical testing in tension indicated that the as-built LPBF permalloy exhibited lower tensile strength and ductility compared with wrought permalloy,[28] a behavior primarily attributed to the presence of solidification cracking. Fractographic analysis of as-built specimens revealed mixed-mode fracture initiating at crack surfaces, confirming that these pre-existing microcracks act as effective stress concentrators. The persistence of limited ductility after annealing, despite dissolution of the cellular microstructure and a reduction in defect density, supports the conclusion that solidification crack propagation remains the dominant failure mechanism. The predominantly intergranular fracture morphology, together with Mo- and Fe-rich precipitates in annealed specimens (Figure 10D), further suggests that localized Mo enrichment promotes the formation of brittle secondary phases, such as μ-phase,[12] which would restrict plastic deformation.

Beyond their mechanical implications, secondary phases also impede magnetic domain-wall motion, analogous to dislocation pinning, thereby degrading soft magnetic performance. Accordingly, heat treatments

providing greater thermal exposure (i.e., higher temperature and/or longer duration) than those used for conventionally processed permalloy may be necessary to achieve sufficient homogenization of the compositional segregation characteristic of LPBF microstructures.

Additionally, LPBF permalloy samples in both the as-printed and annealed conditions exhibited clear soft-ferromagnetic hysteresis behavior, as shown in Figure 11. However, the absolute magnetic property values reported here should be interpreted with caution, given the sensitivity of soft-magnetic measurements to sample geometry, surface preparation, demagnetization corrections, and the limited low-field resolution of the VSM technique.[45,46]

Within these constraints, the annealed specimens were more readily magnetized than the as-printed counterparts, as evidenced by the steeper initial slope of the hysteresis loop near H = 0 A/m, and the reduction in coercivity from 83 A/m to 10 A/m after heat treatment. This response is consistent with annealing-induced microstructural changes, including dissolution of the cellular solidification structure, relief of residual stresses, and decreased dislocation density, all of which facilitate magnetic domain wall motion.

Despite these improvements, LPBF-related defects such as residual porosity, microcracks, and impurity segregation persist and would continue to limit ideal soft-magnetic performance by acting as domain-wall pinning sites.[47,48] Consequently, the observed enhancement in initial magnetization and coercivity should be interpreted primarily as a comparative indicator of microstructural recovery rather than an absolute measure of optimized magnetic performance. The reduction in saturation magnetization relative to the wrought condition is also qualitatively consistent with the lower relative density, increased impurity content, and the development of a pronounced <200> crystallographic texture, which corresponds to a comparatively hard magnetization axis in FCC Ni-based alloys.[19]

5. Conclusion

In this study, Ni–Fe–Mo permalloy was investigated as a candidate alloy for LPBF with a goal of enabling additively manufactured magnetic-shielding components. A systematic processing study spanning a broad range of laser powers and scan speeds was conducted to identify the LPBF parameter set that maximizes density while minimizing susceptibility to solidification (hot) cracking. Process mapping indicated that a laser power of 200 W combined with a scan speed of 900 mm/s provided the most favorable balance among melt-pool stability, defect suppression, and part densification. Under these conditions, a relative density of 99.65% was achieved while minimizing microcrack formation.

Microstructural characterization of the as-built material revealed a pronounced (200) crystallographic preferred orientation along the build direction and a fine cellular segregation structure, both characteristic of Ni-based alloys processed by LPBF. These features were substantially reduced through post-build annealing, which produced a more homogeneous microstructure consistent with residual stress relief and improved magnetic response.

Mechanical testing demonstrated that additively manufactured permalloy exhibited lower tensile strength and ductility than its wrought counterpart, behavior primarily attributed to residual microcracks that persisted in small amounts (e.g., ~1 per mm). Initial magnetic characterization confirmed that the alloy retained desirable soft-magnetic behavior, which was further improved following post-process annealing.

This study demonstrated that permalloy can be successfully processed by LPBF and remains a promising candidate for high-performance magnetic-shielding applications. Nevertheless, the minor presence of solidification cracking remains a key challenge. Achieving mechanical and magnetic properties competitive with conventionally processed material will require not only further optimization of LPBF processing parameters, but also secondary densification and homogenization treatments, such as HIP, to remove microstructural defects and compositional segregation.

Acknowledgements

The authors gratefully acknowledge Mr. Henri Baldino, Dr. Daniel Hedlund, and Dr. Piotr Kulik at the University of Central Florida for their valuable technical contributions, insightful discussions, and continued collaboration throughout the course of this work. The authors also thank Mr. Kirk Scammon of the UCF Materials Characterization Facility (MCF) for providing training in materials characterization techniques.

Funding

This study was funded by Philips Medical Systems (grant number: 8600136118) and the Florida High Tech Corridor Council (grant number: 2026-004).

Conflicts of interest

Yongho Sohn serves as an Editorial Board Member of the journal but was not in any way involved in the editorial and peer-review process conducted for this paper, directly or indirectly. The other authors declare they have no

competing interests. In addition, the views, opinions, and conclusions made in this document are those of the authors and should not be interpreted as representing the official policies, either expressed or implied, of Philips Medical Systems.

Author contributions

Conceptualization: Nicolas Ayers, Yongho Sohn
Data curation: Nicolas Ayers
Formal analysis: Nicolas Ayers
Funding acquisition: Yongho Sohn
Investigation: Nicolas Ayers, Nemanja Kljestan, Saeyeong Jeon
Methodology: Nicolas Ayers, Yongho Sohn
Resources: Marko Knezevic, Yong Kyu Yoon, Yongho Sohn
Supervision: Marko Knezevic, Yong Kyu Yoon, Yongho Sohn
Visualization: Nicolas Ayers
Writing–original draft: Nicolas Ayers
Writing–review & editing: Nicolas Ayers, Saeyeong Jeon, Marko Knezevic, Yongho Sohn

Ethics approval and consent to participate

Not applicable.

Consent for publication

Not applicable.

Availability of data

All data associated with this publication are available upon reasonable request from the corresponding author.

References

1. Jiles D. Recent advances and future directions in magnetic materials. *Acta Mater*. 2003;51(19):5907-5939.

   doi: 10.1016/j.actamat.2003.08.011

2. O'Handley RC. *Modern Magnetic Materials: Principles and Applications*. 1st ed. New York, NY: John Wiley & Sons, Inc.; 2000.

3. Chikazumi S, Graham CD. *Physics of Ferromagnetism*. 2nd ed. Oxford, UK: Oxford University Press; 1997.

4. Xu X, Liu W, Huang Y, *et al*. Magnetic shielding mechanism and structure design of composites at low frequency: A review. *J Magn Magn Mater*. 2023;570:170509.

   doi: 10.1016/j.jmmm.2023.170509

5. Sun J, Ren J, Li J, *et al*. Measurement and analysis of magnetic properties of permalloy for magnetic shielding devices under different temperature environments. *Materials*. 2023;16(8):3253.

   doi: 10.3390/ma16083253

6. Song YL, Lin HY, Manikandan S, *et al*. A magnetic field canceling system design for diminishing electromagnetic interference to avoid environmental hazard. *Int J Environ Res Public Health*. 2022;19(6):3664.

   doi: 10.3390/ijerph19063664

7. Kim ES, Haftlang F, Ahn SY, *et al*. Effects of processing parameters and heat treatment on the microstructure and magnetic properties of the in-situ synthesized Fe-Ni permalloy produced using direct energy deposition. *J Alloys Compd*. 2022;907:164415.

   doi: 10.1016/j.jallcom.2022.164415

8. Rodriguez-Vargas BR, Stornelli G, Folgarait P, *et al*. Recent advances in additive manufacturing of soft magnetic materials: A review. *Materials*. 2023;16(16):5610.

   doi: 10.3390/ma16165610

9. Hasselgren L, Luomi J. Geometrical aspects of magnetic shielding at extremely low frequencies. *IEEE Trans Electromagn Compat*. 1995;37(3):409-420.

   doi: 10.1109/15.406530

10. Narasimharaju SR, Zeng W, See TL, *et al*. A comprehensive review on laser powder bed fusion of steels: Processing, microstructure, defects and control methods, mechanical properties, current challenges and future trends. *J Manuf Process*. 2022;75:375-414.

    doi: 10.1016/j.jmapro.2021.12.033

11. Liu G, Zhang X, Chen X, *et al*. Additive manufacturing of structural materials. *Mater Sci Eng R Rep*. 2021;145:100596.

    doi: 10.1016/j.mser.2020.100596

12. Haines MP, Rielli VV, Primig S, *et al*. Powder bed fusion additive manufacturing of Ni-based superalloys: a review of the main microstructural constituents and characterization techniques. *J Mater Sci*. 2022;57(30):14135-14187.

    doi: 10.1007/s10853-022-07501-4

13. Hyer H, Zhou L, Park S, *et al*. Understanding the laser powder bed fusion of AlSi10Mg alloy. *Metallogr Microstruct Anal*. 2020;9(4):484-502.

    doi: 10.1007/S13632-020-00659-W

14. Diaz Vallejo N, Lucas C, Ayers N, *et al*. Process optimization and microstructure analysis to understand laser powder bed fusion of 316L stainless steel. *Metals*. 2021;11(5):832.

    doi: 10.3390/met11050832

15. Ayers N, Lucas C, Mahmud A, *et al*. Parameter Optimization and Flaw Type Dependent Tensile Properties of 15-5PH Stainless Steel Manufactured by Laser Powder Bed Fusion. *Adv Eng Mater*. 2024;26(23).

    doi: 10.1002/adem.202401346

16. Cao S, Zou Y, Lim CVS, *et al*. Review of laser powder bed fusion (LPBF) fabricated Ti-6Al-4V: process, post-process

treatment, microstructure, and property. *Light: Adv Manuf*. 2021;2(3):313-332.

doi: 10.37188/lam.2021.020

17. Huynh T, Mehta A, Graydon K, *et al*. Microstructural development in Inconel 718 nickel-based superalloy additively manufactured by laser powder bed fusion. *Metallogr Microstruct Anal*. 2022;11(1):88-107.

doi: 10.1007/S13632-021-00811-0

18. Mehta A, Zhou L, Huynh T, *et al*. Additive manufacturing and mechanical properties of the dense and crack free Zr-modified aluminum alloy 6061 fabricated by the laser-powder bed fusion. *Addit Manuf*. 2021;41:101966.

doi: 10.1016/j.addma.2021.101966

19. Mohamed AEMA, Zou J, Sheridan RS, *et al*. Magnetic shielding promotion via the control of magnetic anisotropy and thermal Post processing in laser powder bed fusion processed NiFeMo-based soft magnet. *Addit Manuf*. 2020;32:101079.

doi: 10.1016/j.addma.2020.101079

20. Zou J, Gaber Y, Voulazeris G, *et al*. Controlling the grain orientation during laser powder bed fusion to tailor the magnetic characteristics in a Ni-Fe based soft magnet. *Acta Mater*. 2018;158:230-238.

doi: 10.1016/j.actamat.2018.07.064

21. Yang J, Tian Y, Wang Z, *et al*. Research on the anisotropy of soft magnetic performance of SLM-fabricated NiFeMo alloys. *J Alloys Compd*. 2025;1018:179264.

doi: 10.1016/j.jallcom.2025.179264

22. Li B, Fu WQ, Xu HS, *et al*. Additively manufactured Ni-15Fe-5Mo Permalloy via selective laser melting and subsequent annealing for magnetic-shielding structures: Process, microstructural and soft-magnetic characteristics. *J Magn Magn Mater*. 2020;494:165754.

doi: 10.1016/j.jmmm.2019.165754

23. Mohamed AEMA, Sheridan RS, Bongs K, *et al*. Microstructure-magnetic shielding development in additively manufactured Ni-Fe-Mo soft magn*et al*loy in the as fabricated and post-processed conditions. *J Alloys Compd*. 2021;884:161112.

doi: 10.1016/j.jallcom.2021.161112

24. Marchese G, Basile G, Bassini E, *et al*. Study of the microstructure and cracking mechanisms of hastelloy X produced by laser powder bed fusion. *Materials*. 2018;11(1):106.

doi: 10.3390/ma11010106

25. Tomus D, Jarvis T, Wu X, *et al*. Controlling the microstructure of Hastelloy-X components manufactured by selective laser melting. *Phys Procedia*. 2013;41:823-827.

doi: 10.1016/j.phpro.2013.03.154

26. Razee SSA, Staunton JB, Ginatempo B, *et al*. Ab Initio theoretical description of the interrelation between magnetocrystalline anisotropy and atomic short-range order. *Phys Rev Lett*. 1999;82(26):5369.

doi: 10.1103/PhysRevLett.82.5369

27. Vahdati Yekta P, Ghasemi A, Sharifi EM. Magnetic and mechanical properties of cold-rolled permalloy. *J Magn Magn Mater*. 2018;468:155-163.

doi: 10.1016/j.jmmm.2018.07.088

28. ASTM A753-21 Standard Specification for Wrought Nickel-Iron Soft Magnetic Alloys. ASTM International; 2021.

29. Yang J, Zhu Q, Wang Z, *et al*. Effects of metallurgical defects on magnetic properties of SLM NiFeMo permalloy. *Mater Charact*. 2023;197:112672.

doi: 10.1016/j.matchar.2023.112672

30. Bahl CRH. Estimating the demagnetization factors for regular permanent magnet pieces. *AIP Advances*. 2021;11(7).

doi: 10.1063/5.0060897

31. Aharoni A. Demagnetizing factors for rectangular ferromagnetic prisms. *J Appl Phys*. 1998;83(6):3432-3434.

doi: 10.1063/1.367113

32. Zhao Y, Ma Z, Yu L, *et al*. New alloy design approach to inhibiting hot cracking in laser additive manufactured nickel-based superalloys. *Acta Mater*. 2023;247:118736.

doi: 10.1016/j.actamat.2023.118736

33. Zhao C, Parab ND, Li X, *et al*. Critical instability at moving keyhole tip generates porosity in laser melting. *Science*. 2020;370(6520):1080-1086.

doi: 10.1126/science.abd1587

34. Afrasiabi M, Keller D, Lüthi C, *et al*. Effect of process parameters on melt pool geometry in laser powder bed fusion of metals: a numerical investigation. *Procedia CIRP*. 2022;113:378-384.

doi: 10.1016/j.procir.2022.09.187

35. Song X, Zhang W, Liu Z, *et al*. Microstructures and cracking behaviors of AlCoCrFeNiTi0.2 high-entropy alloy fabricated by laser powder bed fusion. *J Alloys Compd*. 2025;1031:180999.

doi: 10.1016/j.jallcom.2025.180999

36. Platl J, Bodner S, Hofer C, *et al*. Cracking mechanism in a laser powder bed fused cold-work tool steel: The role of residual stresses, microstructure and local elemental concentrations. *Acta Mater*. 2022;225:117570.

doi: 10.1016/j.actamat.2021.117570

37. Wang DZ, Li KL, Yu CF, *et al*. Cracking behavior in additively manufactured pure tungsten. *Acta Metall Sin (Engl Lett)*.

2018;32(1):127-135.

doi: 10.1007/s40195-018-0752-2

38. Wang N, Mokadem S, Rappaz M, *et al*. Solidification cracking of superalloy single-and bi-crystals. *Acta Mater*. 2004;52(11):3173-3182.

doi: 10.1016/j.actamat.2004.03.047

39. Kou S. *Welding Metallurgy*. 2nd ed. New York, NY: John Wiley & Sons; 2003.

40. Kou S. A criterion for cracking during solidification. *Acta Mater*. 2015;88:366-374.

doi: 10.1016/j.actamat.2015.01.034

41. Higashi M, Ozaki T. Selective laser melting of pure molybdenum: Evolution of defect and crystallographic texture with process parameters. *Mater Des*. 2020;191:108588.

doi: 10.1016/j.matdes.2020.108588

42. Hyer H, Zhou L, Mehta A, *et al*. Composition-dependent solidification cracking of aluminum-silicon alloys during laser powder bed fusion. *Acta Mater*. 2021;208:116698.

doi: 10.1016/j.actamat.2021.116698

43. Yakubu S. Domain and Domain Wall Motion. *Ferroic Materials-Understanding, Development, and Utilization*. 2025.

doi: 10.5772/intechopen.1006892

44. Li C, Ruan H, Chen D, *et al*. Effect of heat treatment on the microstructure and properties of Ni based soft magnetic alloy. *Microsc Res Tech*. 2018;81(7):796-802.

doi: 10.1002/jemt.23038

45. Fiorillo F. Measurements of magnetic materials. *Metrologia*. 2010;47(2):S114-S142.

doi: 10.1088/0026-1394/47/2/S11

46. Dodrill B, Lindemuth JR. Vibrating sample magnetometry. In: *Magnetic Measurement Techniques for Materials Characterization*. New York, NY: Springer International Publishing; 2021:15-37.

doi: 10.1007/978-3-030-70443-8_2

47. Sun Y, Hebert RJ, Aindow M. Non-metallic inclusions in 17-4PH stainless steel parts produced by selective laser melting. *Mater Des*. 2018;140:153-162.

doi: 10.1016/j.matdes.2017.11.063

48. Callister WD, Rethwisch DG, Blicblau A, *et al*. *Materials Science and Engineering: An Introduction*. 7th ed. New York, NY: John Wiley & Sons; 2007.